JCB Journal of Cell Biology

REPORT

A role for Vps13-mediated lipid transfer at the ER–endosome contact site in ESCRT-mediated sorting

Sho W. Suzuki[1,3], Matthew West[2], Yichen Zhang[1], Jenny S. Fan[1], Rachel T. Roberts[1], Greg Odorizzi[2], and Scott D. Emr[1]

Endosomes are specialized organelles that function in the secretory and endocytic protein sorting pathways. Endocytosed cell surface receptors and transporters destined for lysosomal degradation are sorted into intraluminal vesicles (ILVs) at endosomes by endosomal sorting complexes required for transport (ESCRT) proteins. The endosomes (multivesicular bodies, MVBs) then fuse with the lysosome. During endosomal maturation, the number of ILVs increases, but the size of endosomes does not decrease despite the consumption of the limiting membrane during ILV formation. Vesicle-mediated trafficking is thought to provide lipids to support MVB biogenesis. However, we have uncovered an unexpected contribution of a large bridge-like lipid transfer protein, Vps13, in this process. Here, we reveal that Vps13-mediated lipid transfer at ER–endosome contact sites is required for the ESCRT pathway. We propose that Vps13 may play a critical role in supplying lipids to the endosome, ensuring continuous ESCRT-mediated sorting during MVB biogenesis.

Introduction

Intracellular organelles in eukaryotic cells are essential for compartmentalizing various biochemical and cell signaling reactions. Cells utilize specific vesicle-mediated trafficking systems to populate these organelles with unique sets of protein constituents that carry out these reactions. The ESCRTs (ESCRT-0, -I, -II, -III, and Vps4 AAA-ATPase) sort cell-surface receptors and membrane proteins into vesicles that invaginate and bud into the lumen of the late endosome (forming multivesicular bodies, MVBs) (Henne et al., 2011). These MVBs then fuse with the lysosome (the vacuole in yeast) delivering the membrane protein–containing vesicle into the lumen of the lysosome, where they are degraded. In addition to MVB formation, the ESCRTs mediate other critical cellular processes, including the budding of enveloped viruses, such as HIV, cytokinesis, plasma membrane repair, extracellular vesicle formation, and nuclear envelope reformation (Lee et al., 2007; Rusten et al., 2007; Carlton et al., 2008; Hurley, 2015). ESCRT dysfunction has been implicated in numerous diseases, including cancer, neurodegeneration, Huntington's disease, and Parkinson's disease (Saksena and Emr, 2009).

Vps13 belongs to a family of lipid transfer proteins that function at various membrane contact sites (Ugur et al., 2020; Dziurdzik and Conibear, 2021; Melia and Reinisch, 2022; Neuman et al., 2022). These large proteins (>3,000 AA) have been proposed to bridge membranes to form a direct channel for non-selective lipid transport between two different organelles. The human genome encodes four VPS13 homologs (VPS13A-D), each of which localizes to distinct membrane contact sites. For instance, VPS13A localizes to the ER–mitochondria contact site (Kumar et al., 2018; Yeshaw et al., 2019; Muñoz-Braceras et al., 2019), whereas VPS13C localizes to the ER–endosome contact site (Kumar et al., 2018). Mutations in VPS13 homologs have been associated with a variety of neurological disorders, including chorea acanthocytosis (VPS13A) (Rampoldi et al., 2001), Cohen syndrome (VPS13B) (Kolehmainen et al., 2003), Parkinson's disease (VPS13C) (Lesage et al., 2016), and ataxia (VPS13D) (Seong et al., 2018; Gauthier et al., 2018). Yeast has a single Vps13 that localizes to multiple organelles and membrane contact sites (Dziurdzik and Conibear, 2021). Upon sporulation, Vps13 localizes to the ER–prospore membrane contact site to support spore membrane expansion (Park and Neiman, 2012; Nakamura et al., 2021). Under glucose limitation, it is enriched at the nucleus–vacuole junction (NVJ) (Bean et al., 2018; Lang et al., 2015; Park et al., 2016). It also localizes at the ER–peroxisome and ER–autophagosome contact sites that function in peroxisome and autophagosome biogenesis, respectively (Yuan et al., 2022;

[1]Weill Institute for Cell and Molecular Biology and Department of Molecular Biology and Genetics, Cornell University, Ithaca, NY, USA; [2]Molecular, Cellular and Developmental Biology, University of Colorado, Boulder, CO, USA; [3]School of Biological Sciences, Nanyang Technological University, Singapore.

Correspondence to Sho W. Suzuki: sho.suzuki@ntu.edu.sg.

Dabrowski et al., 2023). During cell proliferation, Vps13 primarily localizes to the endosome (Bean et al., 2018; Park et al., 2016; Rzepnikowska et al., 2017). However, the precise function of Vps13 at the endosome remains unclear. Here, we provide evidence that Vps13 forms a lipid transfer channel at the ER–endosome contact site, which is critical for ESCRT-mediated sorting.

Results and discussion

Vps13 is required for efficient ESCRT-mediated sorting

During endosome maturation, the number of intraluminal vesicles (ILVs) increases. Each endosome contains 60–70 vesicles in yeast. Although the endosomal limiting membrane is consumed to form ILVs, the endosome does not shrink. Vesicle-mediated transport is thought to provide lipids to support MVB biogenesis, but it has not been experimentally tested. To characterize its molecular details, we re-examined the original data from the vacuolar protein sorting (*vps*) mutants, which were isolated because of their defects in the sorting of carboxypeptidase Y (CPY), a soluble vacuolar hydrolase (Robinson et al., 1988). All ESCRT mutants among the original *vps* collection (i.e., *vps4*, *did4*, *vps24*, *vps27*, *vps20*, *vps22*, *vps25*, *vps28*, *snf7*, *vps23*, and *bro1*) exhibited mild sorting defects (Fig. S1 A). Notably, *vps13* mutants also exhibited a defect similar to that of the ESCRT mutants. Based on this phenotypic similarity, we hypothesized that Vps13 may function in the ESCRT pathway.

To test this, we examined the sorting of Mup1, a methionine permease localized to the plasma membrane (PM) (Menant et al., 2006). Upon methionine stimulation, Mup1 is endocytosed and sorted into ILVs at the endosome by ESCRTs (Fig. 1 A). Then, it is delivered to the vacuole lumen. To evaluate Mup1 sorting, we expressed a GFP-fused Mup1 in yeast cells. In WT cells, Mup1–GFP localized to the PM, but after methionine stimulation, it was sorted into the vacuole lumen (Fig. 1 B). In contrast, Mup1–GFP was barely sorted in *vps13*Δ cells. It accumulated at punctate structures and the vacuole membrane. The vacuolar delivery of Mup1–GFP results in vacuolar protease-resistant GFP fragments that can be detected by immunoblotting. After 90 min of methionine stimulation, Mup1–GFP was fully processed and GFP fragments were observed in WT cells, whereas the majority of Mup1–GFP remained as a stable hybrid protein in *vps13*Δ cells (Fig. 1, C and D), suggesting that Vps13 is required for Mup1 sorting. Note that a small portion of processed GFP (28%) was observed, indicating that Mup1–GFP was still partially sorted even in *vps13*Δ cells. We also examined the sorting of carboxypeptidase S (CPS), another cargo of the ESCRT pathway that is delivered from the Golgi and sorted into ILVs (Fig. 1, E and F). Like Mup1–GFP, GFP–CPS was poorly sorted, leading to its accumulation at punctate structures and the vacuole membrane in *vps13*Δ cells. To further investigate if cargoes were sorted into ILVs in *vps13*Δ cells, we fused a pH-sensitive GFP, pHluorin, to Mup1 (Miesenböck et al., 1998). When Mup1–pHluorin is internalized into the ILV, the pHluorin fluorescence is quenched, which allows us to evaluate the status of cargo sorting at the endosome (Fig. 1 G). After 30 min of stimulation, Mup1–pHluorin was endocytosed to the endosome (Fig. 1, H and I). At 90 min of stimulation, the pHluorin fluorescence was largely quenched, confirming the sorting of Mup1-pHluorin into ILVs in WT cells. In contrast, in *vps13*Δ cells, even after 90 min stimulation, the pHluorin signal was still observed at the endosome, suggesting that Mup1–pHluorin sorting into ILVs was impaired in *vps13*Δ cells. These observations indicate that Vps13 is required for efficient ESCRT-mediated sorting.

Endosome–vacuole fusion is partially impaired in *vps13*Δ cells

In *vps13*Δ cells, both Mup1–GFP and GFP–CPS accumulated at endosomes (Fig. 1, B and E). Since defects in ESCRT activity result in impaired endosome–vacuole fusion (Russell et al., 2012), we examined endosome–vacuole fusion. For this purpose, we monitored the transport of Pep4, a vacuolar hydrolase that is delivered from the Golgi to the vacuole through the endosome (Fig. S1 B). In WT cells, Pep4-GFP was observed in the vacuole lumen, whereas its sorting was severely compromised in *vps45*Δ cells, which have a defect in vesicle fusion with the endosome (Fig. S1, C and D). In ESCRT-deficient *vps4*Δ cells, Pep4-GFP accumulated at punctate structures, reflecting an impairment in endosome–vacuole fusion. In *vps13*Δ cells, we observed vacuole lumen localization, but also several punctate structures outside of the vacuole. The sorting of Pep4 to the vacuole can be monitored by the appearance of the mature form of Pep4 (mPep4) (Fig. S1 E). Indeed, in *vps45*Δ cells, mPep4 was barely detectable, leading to the accumulation of the precursor form of Pep4 (prPep4). In *vps13*Δ cells, although mPep4 was observed, prPep4 accumulated. These results suggest that vacuole transport of Pep4 was partially impaired in *vps13*Δ cells. We also examined the vacuole delivery of Vph1 (Fig. S1 B). Vph1 is a vacuole membrane protein, which functions as a subunit of the vacuolar ATPase. Like Pep4, Vph1 is also delivered to the vacuole through the endosome. In WT cells, Vph1-mCherry colocalized with another vacuole membrane protein, Pho8, directly delivered from the Golgi to the vacuole via the AP-3 pathway (Fig. S1, F and G). In contrast, in *vps45*Δ and *vps4*Δ cells, Vph1-mCherry accumulated at punctate structures, whereas GFP–Pho8 was delivered to the vacuole. In *vps13*Δ cells, Vph1-mCherry not only showed a partial vacuole localization but also several punctate structures. These results suggest that endosome–vacuole fusion is partially impaired in *vps13*Δ cells.

Vps13 is dispensable for retromer-mediated endosomal recycling

To ask whether Vps13 is specifically required for ESCRT-mediated sorting, we examined its role in endosomal recycling. Vps10 is a transmembrane protein receptor for CPY. After delivery to the endosome, Vps10 is recycled back to the Golgi by the retromer coat complex, which enables Vps10 to carry out another round of CPY sorting at the Golgi (Fig. S1 B; Marcusson et al., 1994; Seaman et al., 1997; Seaman et al., 1998). Vps10–GFP localized to punctate structures, which were previously reported to be Golgi or endosomes (Fig. 1, J and K; Marcusson et al., 1994). In *vps35*Δ cells, retromer-mediated endosome-to-Golgi retrograde trafficking is impaired, resulting in the accumulation of Vps10-GFP at the vacuole membrane. In *vps13*Δ cells, Vps10-GFP was still localized to the punctate

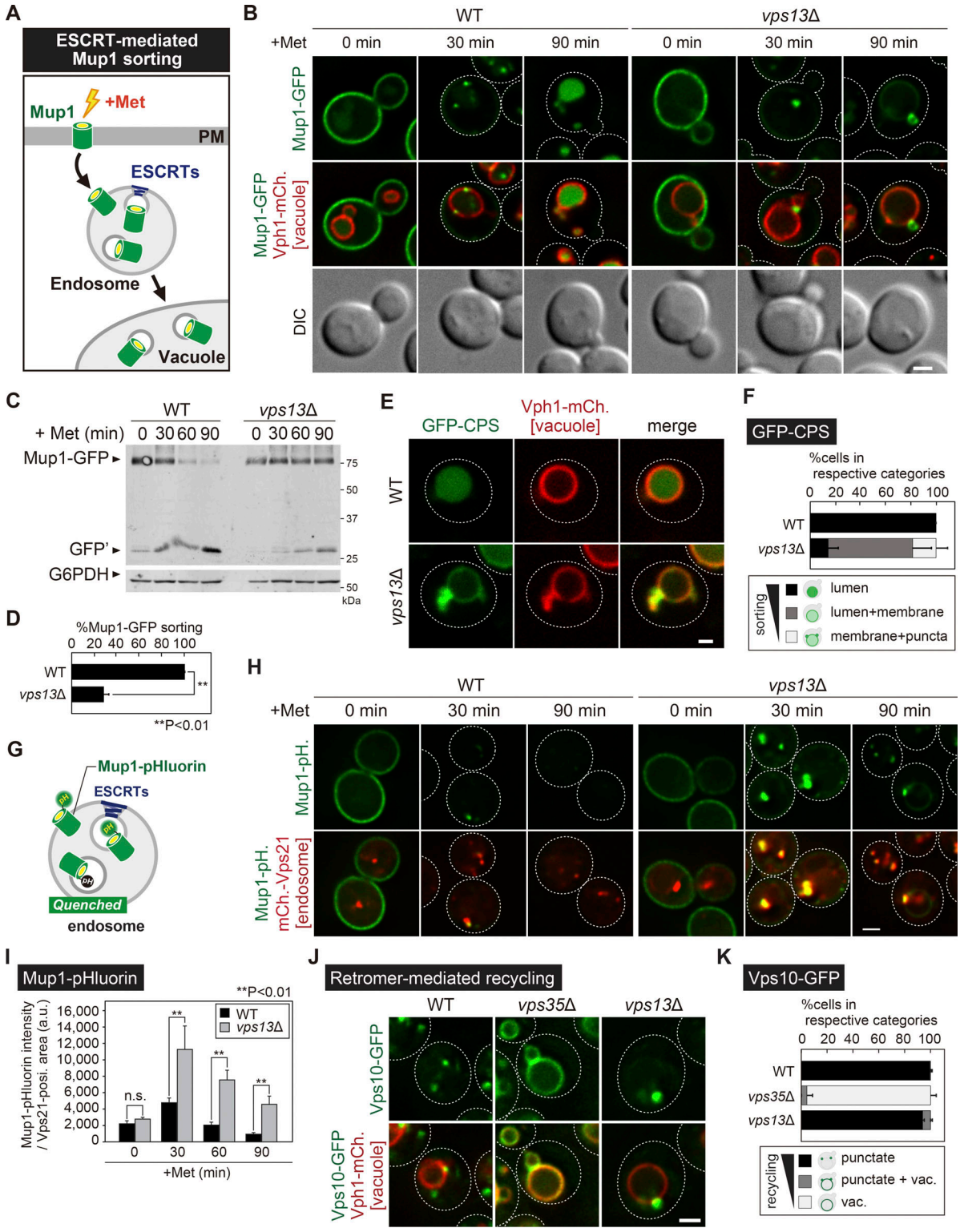

Figure 1. **Vps13 is required for the ESCRT pathway. (A)** Schematic of Mup1 sorting. **(B)** Mup1–GFP localization after methionine stimulation. **(C)** Western blotting analysis of Mup1 sorting. Cell lysates were analyzed by immunoblotting using anti-GFP and anti-G6PDH antibodies. Vacuole delivery of Mup1–GFP yields protease-resistant GFP fragments (GFP'). **(D)** Quantification of Mup1–GFP processing from C. **(E)** GFP–CPS localization. **(F)** Quantification of GFP–CPS localization of each category from E. **(G)** Schematic of Mup1–pHluorin assay. **(H)** Mup1–pHluorin localization after methionine stimulation. **(I)** Quantification of Mup1–pHluorin fluorescence at endosomes from H. **(J)** Vps10–GFP localization in WT, *vps35*Δ (retromer), and *vps13*Δ cells. **(K)** Quantification of Vps10–GFP localization from J. Scale bar: 1 µm. Source data are available for this figure: SourceData F1.

structures (Fig. 1, J and K and Fig. S1 H). We also examined the localization of another retromer cargo, Kex2 (Voos and Stevens, 1998), and its recycling was also not impaired in *vps13*Δ cells (Fig. S1, I and J). These observations suggest that Vps13 is not required for retromer-mediated recycling.

Vps13-mediated lipid transfer at the ER–endosome contact site is critical for the ESCRT pathway

Vps13 is a lipid transfer protein that localizes to various membrane contact sites. It has a characteristic hydrophobic cavity, which is critical for the lipid transfer reaction (Fig. 2, A–C). To define the role of Vps13 in ESCRT-mediated sorting, we examined its localization. Consistent with previous reports (Bean et al., 2018; Park et al., 2016; Rzepnikowska et al., 2017), endogenously expressed Vps13–GFP formed punctate structures, which colocalized with mCherry–Vps21 (Rab5 homolog), confirming its endosomal localization (Fig. S2, A and B). Approximately 10% of Vps13–GFP punctate structures did not colocalize with mCherry–Vps21, presumably because Vps13 also localized to another organelle (i.e., mitochondria, vacuole) as previously reported (Dziurdzik and Conibear, 2021). Vps13 consists of the Extended Chorein, VAB, APT, ATG2_C, and PH domains (Fig. 2 A; Melia and Reinisch, 2022). Since the VAB domain is critical for organelle targeting (Bean et al., 2018), we truncated the C-terminal region including the VAB domain. This mutant (Δ1852–3144) lost endosomal localization (Fig. S2, C and D), indicating that the C-terminal region of Vps13 is required for association with the endosome.

Atg2 is also a bridge-like lipid transfer protein that localizes to the ER-autophagosome contact where it provides phospholipids to support autophagosome formation (Osawa et al., 2019; Valverde et al., 2019). The N-terminal 46 residues of Atg2 are sufficient for association with ER membranes, and this region can be replaced by the N-terminal 39 residues of Vps13 (Kotani et al., 2018). Therefore, we fused GFP to the N-terminal region of Vps13 ($Vps13^{1–39}$-GFP) and examined its localization. Consistent with previous work (Nakamura et al., 2021), $Vps13^{1–39}$-GFP colocalized with the DsRed-HDEL labeled ER (Fig. S2, E and F), suggesting that the N-terminal region of Vps13 is sufficient for association with the ER membrane.

In humans, VPS13C, a paralog of yeast Vps13, has been shown to localize at ER–endosome contact sites (Kumar et al., 2018). Since the N- and C-terminal regions of yeast Vps13 are required for its association with ER and endosomal membranes, we examined whether yeast Vps13 also localizes to ER–endosome contact sites. For this purpose, we generated yeast cells expressing Vps13–GFP, DsRed–HDEL (ER), and Mup1–BFP. After 30 min of methionine stimulation, Mup1–BFP was endocytosed to the endosome (Fig. S2 G). These Mup1–BFP labeled endosomes were frequently observed in close proximity to the ER, which corresponds to ER–endosome contact sites (Fig. 2, D and E; and Fig. S2 G). Notably, Vps13–GFP was enriched at these ER–endosome contact sites (Fig. 2, D, F, and G; and Fig. S2 G). We further analyzed the ER–endosome contact by live-cell imaging and realized that some endosomes dynamically associate and dissociate from the ER membrane (Fig. S2 H). Therefore, we analyzed Vps13–GFP localization in ESCRT mutants, which exhibit a defect in MVB biogenesis. In ESCRT-defective *vps4*Δ cells, the endosomes were swollen and often observed in close proximity to the ER (Fig. 2, D and E). Vps13–GFP was highly enriched at ER–endosome contact sites in this mutant (Fig. 2, D and F). Electron tomography and three-dimensional modeling of *vps4*Δ cells revealed that the ER membrane was close to the characteristic flattened endosomal structures (known as class E compartments) (Fig. 2 H and Video 1). These membranes contacting the endosome were designated ER by the observation of its bound ribosomes, dimensions, and staining by high-pressure freezing and electron tomography (Fig. S2 I). Notably, ribosomes were excluded from these associated membranes, which was also observed in other contact sites such as the ER–mitochondria contacts (Friedman et al., 2011; Murley et al., 2013). Collectively, these results indicate that Vps13 is localized at ER–endosome contact sites.

To ask if ER–endosome contact site localization is required for ESCRT-mediated sorting, we constructed several Vps13 truncation mutants and examined Mup1 sorting. When we truncated the C-terminal region of Vps13 (Δ1852–3144), which is required for its endosomal localization, Mup1 sorting was impaired (Fig. 2 I; and Fig. S2 J). Similarly, cells lacking the N-terminal region (Δ2-21, Δ2-32, Δ2-52), required for association with the ER membrane, also exhibited defects in Mup1 sorting. These results suggest that Vps13's association with both the ER and endosome membranes is crucial for the ESCRT pathway.

Vps13 is proposed to bridge two different organelle membranes at a contact site for lipid transport. Consistent with this model, mutations in hydrophobic residues at the Extended Chorein-N domain, responsible for lipid transport, impair sporulation (Fig. 2 C; Li et al., 2020). We examined Mup1 sorting in this lipid transfer mutant (mut1). It exhibited a severe defect comparable with *vps13*Δ cells (Fig. 2, J and K; and Fig. S2, K and L), suggesting that the lipid transfer activity of Vps13 is required for ESCRT-mediated sorting.

Vps13 is not required for cargo ubiquitination and ESCRT recruitment

During ESCRT-mediated sorting, transmembrane cargoes are ubiquitinated and then recognized by ESCRT-0 (Fig. S3 A; Henne et al., 2011). Subsequently, downstream ESCRTs (ESCRT-I, ESCRT-II, ESCRT-III, and Vps4 AAAase) are recruited to the endosomal surface. ESCRT-III forms a unique spiral structure that induces membrane invagination and constriction. Finally, Vps4 catalyzes membrane scission. We sought to determine whether Vps13 is required at a specific stage of ESCRT-mediated sorting.

We first examined the ubiquitination status of ESCRT cargoes in *vps13*Δ cells. We immunoprecipitated Mup1–GFP from methionine-stimulated cells, and we were able to detect ubiquitinated forms of Mup1–GFP even in *vps13*Δ cells (Fig. S3 B). To further investigate the requirement of Vps13 in cargo ubiquitination, we used a rapamycin-dependent degradation system (Fig. 3 A; and Zhu et al., 2017). In this system, FKBP-fused cargo proteins and three ubiquitin-conjugated FRBs (FRB-3xUb) are coexpressed. Upon rapamycin treatment, FKBP forms a complex with FRB, which allows ubiquitin recruitment to cargoes. By

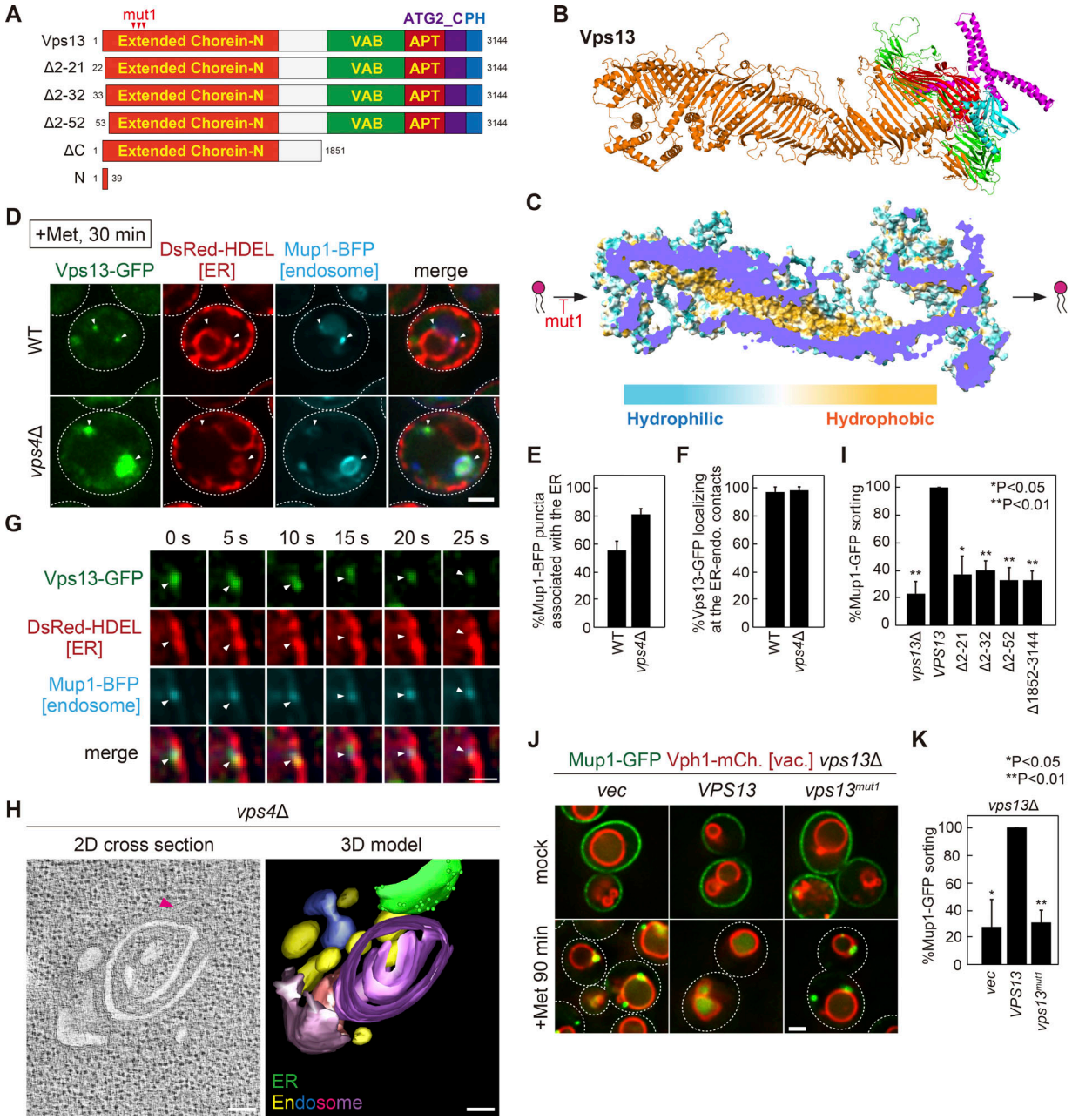

Figure 2. **The ER–endosome contact site localization of Vps13 is critical for ESCRT-mediated sorting. (A)** Schematic of Vps13 mutants. **(B)** The ribbon cartoon of Vps13 was generated using AlphaFold2. **(C)** The surface model of the alphafold predicted structure of Vps13. Blue and yellow indicate hydrophilic and hydrophobic residues, respectively. **(D)** Vps13–GFP localization at the ER–endosome contact site. Vps13–GFP, DsRed–HDEL (ER), and Mup1–BFP (endosome) expressing WT and *vps4*Δ cells were stimulated with methionine for 30 min. Scale bar: 1 µm. **(E)** Quantification of Mup1-BFP puncta associated with the ER (DsRed-HDEL) from D. **(F)** Quantification of Vps13–GFP localization at the ER–endosome contact site from D. **(G)** Live-cell imaging analysis of Vps13–GFP at the ER-endosome contact site. Vps13–GFP, DsRed–HDEL (ER), and Mup1–BFP (endosome) expressing WT cells were stimulated with methionine for 30 min. Scale bar: 500 nm. **(H)** Two-dimensional cross-sections and three-dimensional models of *vps4*Δ cells. ER is traced in green. Ribosomes are indicated as green dots. The endosome stacks are shown in different colors to differentiate individual membranes. Round endosomes are traced in yellow. Larger tubular and cisternal structures are in various shades. Scale bars: 100 nm. **(I and K)** Quantification of Mup1 sorting in *vps13* mutants from Fig. S2, J and K. **(J)** Mup1–GFP localization after methionine stimulation in *vps13* mutants. Scale bar: 1 µm.

doing this, it can induce ESCRT-mediated sorting in a ubiquitin ligase-independent manner. After a 90-minute treatment with rapamycin, Can1-FKBP was efficiently sorted into the vacuole lumen in WT cells, whereas it was poorly sorted in *vps13*Δ cells (Fig. 3, B–D). These results indicate that Vps13 is not required for cargo ubiquitination. We next examined whether ESCRTs are properly localized to the endosome in *vps13*Δ cells. GFP–Vps27 (ESCRT-0), Snf7–GFP (ESCRT-III), and Vps4–GFP were colocalized with the endosome marker mCherry–Vps21, even in *vps13*Δ cells (Fig. 3, E and F; and Fig. S3, C–F), suggesting that Vps13 function may be downstream of ESCRT recruitment. These results suggest that Vps13 is required for ESCRT-mediated

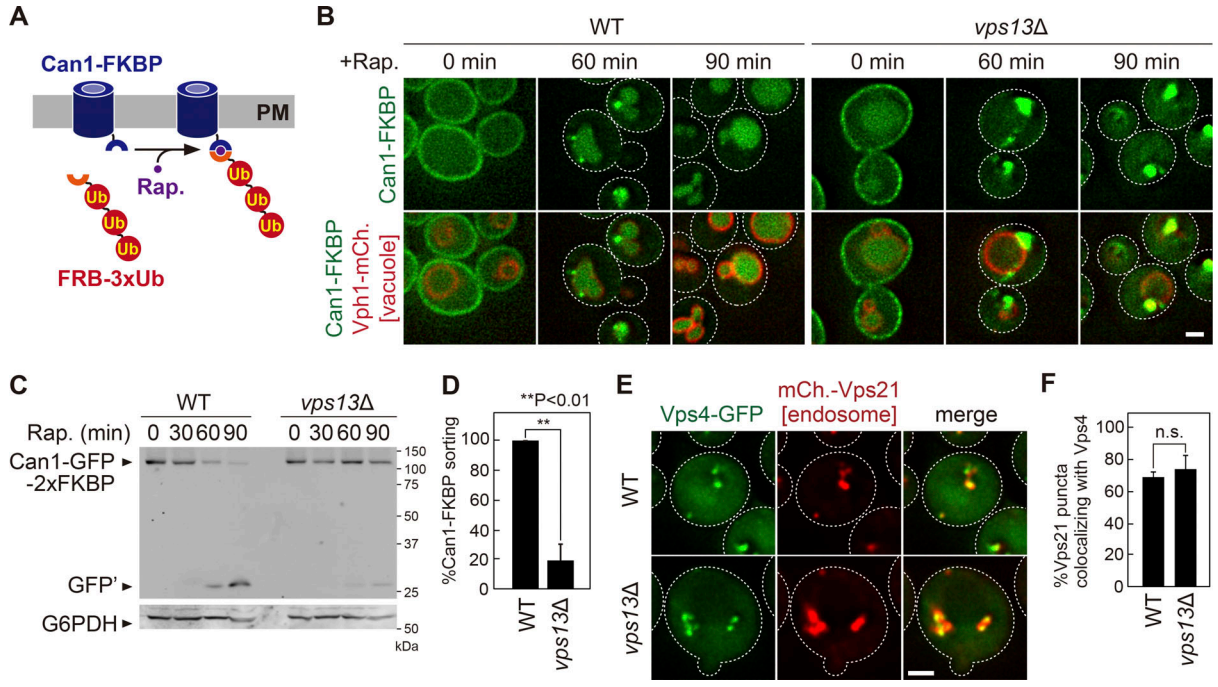

Figure 3. **Vps13 is not required for cargo ubiquitination and ESCRT recruitment. (A)** Schematic of a rapamycin-dependent degradation system for Can1. **(B)** Can1–FKBP localization. Rapamycin-insensitive mutant cells (*tor1-1, fpr1Δ*) expressing Can1–GFP–2xFKBP (Can1–FKBP) and FRB–3xUb were treated with rapamycin. **(C)** Can1–FKBP processing after rapamycin treatments. Cell lysates were analyzed by immunoblotting using anti-GFP and anti-G6PDH antibodies. **(D)** Quantification of Can-FKBP sorting from C. **(E)** Vps4–GFP localization. **(F)** Quantification of endosomal Vps4–GFP localization from E. Scale bar: 1 µm. Source data are available for this figure: SourceData F3.

sorting, but not essential for cargo ubiquitination and ESCRT recruitment.

Efficient intraluminal vesicle formation requires Vps13

To investigate ILV formation in *vps13Δ* cells, we employed electron tomography and three-dimensional modeling (Fig. 4 A; and Videos 2, 3, and 4). Consistent with the partial Mup1 sorting (Fig. 1 C), the *vps13Δ* cells displayed spherical endosomal structures containing ILVs (MVBs). Strikingly, these cells exhibited an increased number of MVBs, and these MVBs frequently clustered together (Fig. 4, B and C; and Fig. S3, G–J). Consistent with this observation, fluorescence microscopy also revealed that Vps55-GFP labeled endosomes form clusters in *vps13Δ* cells (Fig. 4 D and Fig. S3 K). The size of endosomes in *vps13Δ* cells was 1.78-fold larger than that of WT cells (Fig. 4 E and Fig. S3 H), while the number of ILVs per endosome was similar (Fig. 4 F and Fig. S3 H). Notably, the size of ILVs in *vps13Δ* cells was 1.34-fold larger and exhibited greater heterogeneity, contrasting with the smaller and more uniform ILVs observed in WT cells (Fig. 4 G and Fig. S3 H). Intriguingly, several ILVs in *vps13Δ* cells exceeded 90 nm in size, which was rarely observed in WT cells. Furthermore, we analyzed the inward budding profile (BP) and found that *vps13Δ* exhibited a lower BP frequency compared with WT cells, although the ILV size is larger (Fig. 4 H and Fig. S3 H). These observations suggest that Vps13 is required for proper ESCRT function at the endosome.

Although BP frequency was lower in *vps13Δ* cells, the number of ILVs per endosome was similar to WT cells, probably because *vps13Δ* cells have a partial defect in endosome–vacuole fusion. Indeed, the *ypt7Δ* cells, which have a defect in endosome–vacuole fusion, exhibited an increased number of MVBs, and the MVB size was larger than that of WT cells (Russell et al., 2012). Hence, we evaluated ILV formation efficiency by monitoring the sorting of NBD-PC (Bilodeau et al., 2002). NBD-PC is delivered to endosomes and specifically incorporated into ILVs through the ESCRT pathway (Fig. 4 I). Subsequently, NBD-PC is delivered into the vacuole lumen (Fig. 4, J and K). In contrast, it was barely delivered to the vacuole lumen and accumulated to the vacuole membrane in *vps13Δ* cells as well as in the Vps13 lipid transfer mutants (*vps13^{mut1}*), suggesting that the consumption of ILV membrane was slower in *vps13Δ* cells. Collectively, these observations indicate that Vps13 is required for efficient ILV formation.

The role of Vps13 in ESCRT-mediated sorting

During MVB formation, the endosome does not shrink, although its limiting membrane is consumed to form ILV. How lipids are supplied to support MVB formation remains an open question. In this study, we found that Vps13 is required for ESCRT-mediated sorting at the endosome. Mutational analysis revealed that Vps13-mediated lipid transfer at the ER–endosome contact site is required for the ESCRT pathway. Cell biological and electron tomography analysis revealed that MVB sorting was impaired in *vps13Δ* cells. Based on these observations, we propose that the limiting membrane of the endosome is consumed during MVB formation, and Vps13 may play a critical role in providing lipids to the endosome that permit continuous ESCRT-mediated sorting (Fig. 5). Strikingly, Atg2, another Vps13-like lipid transfer protein, delivers phospholipids from

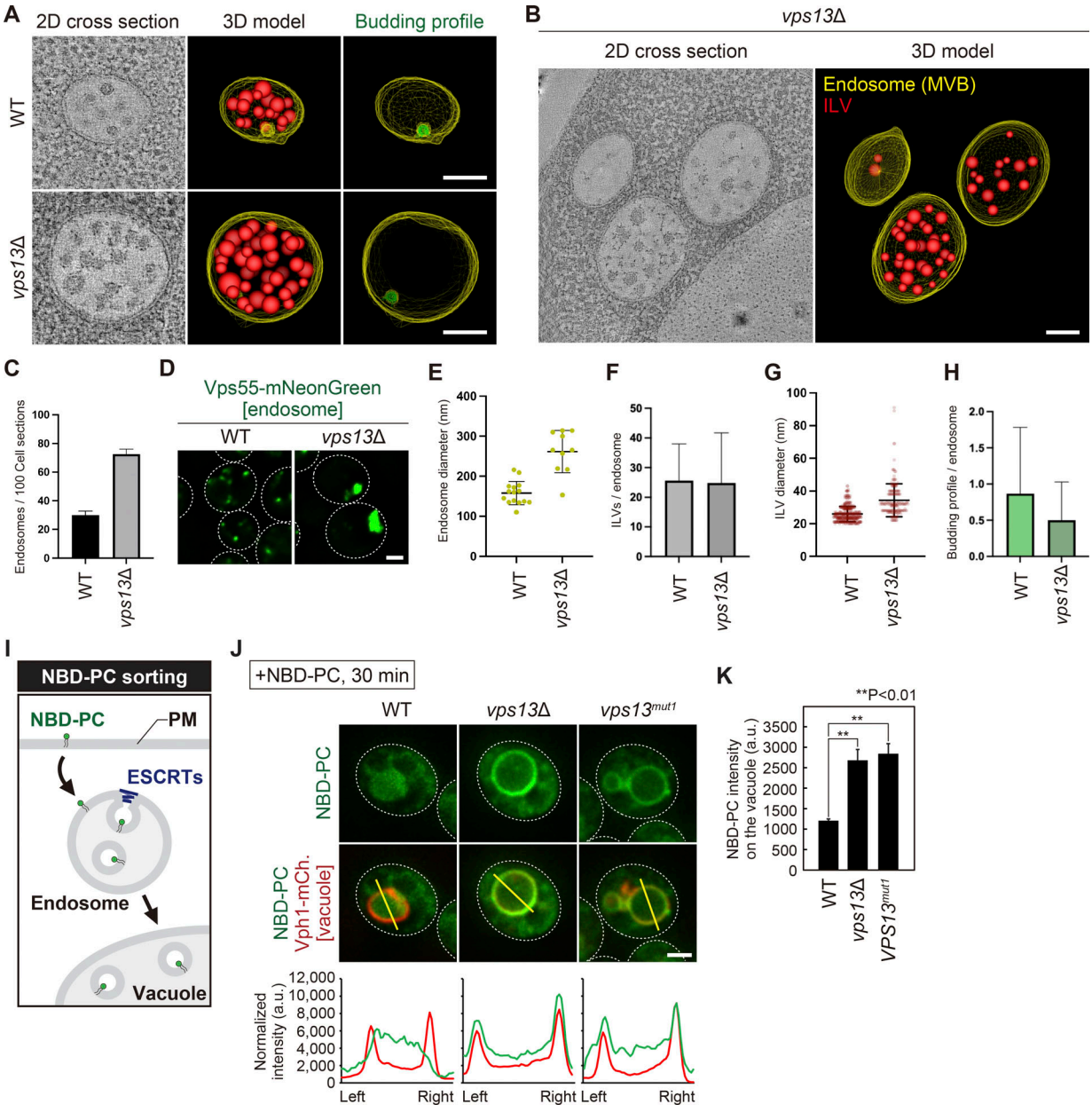

Figure 4. **Efficient intraluminal vesicle formation requires Vps13. (A and B)** Cross-sectional tomographic slices and three-dimensional models of WT and *vps13Δ* cells. Endosome-limiting membranes are traced in yellow, and detached ILVs are traced in red. ILV budding profiles are traced in green. Scale bars: 100 nm. **(C)** Quantification of the number of endosomes. **(D)** Vps55–mNeonGreen localization. Scale bars: 1 µm. **(E)** Measurement of the diameter of endosomes. **(F)** Quantification of the number of ILVs per endosome. **(G)** Measurement of ILV diameter. **(H)** Quantification of the budding profile (BPs) per endosome. The percentage of the limiting membrane incorporated into ILV budding profiles was measured for each strain. **(I)** Schematic of NBD-PC sorting. **(J)** NBD-PC localization after 30 min staining. Scale bars: 1 µm. **(K)** Quantification of NBD-PC intensity at the vacuole membrane.

the ER to the autophagosome to support its expansion (Osawa et al., 2019; Valverde et al., 2019). A similar mechanism may exist in MVB biogenesis.

In this study, we propose that lipids supplied by Vps13 are crucial for ESCRT-mediated sorting, but their precise physiological significance remains unclear. Interestingly, electron tomography and three-dimensional analysis revealed that *vps13Δ* cells exhibited a decrease in ILV budding profiles, an increase in ILV size, and a more heterogeneous size distribution. Maintaining appropriate lipid composition might, therefore, impact the efficiency of ILV formation in addition to being important for ILV cargo sorting by the ESCRT machinery.

Our study sheds light on the critical role of Vps13 in the ESCRT pathway. Human cells possess 10 VPS13-like proteins, including VPS13A/B/C/D, ATG2A/B, Hobbit, Tweek, SHIP164, and UHRF1BP1, all of which function as bridge-like lipid transfer proteins (Toulmay et al., 2022; Levine, 2022). These proteins not only localize to the ER–endosome contact site but also to various other sites, including those between the ER and PM, lysosomes, and autophagosomes. Interestingly, ESCRTs function on diverse

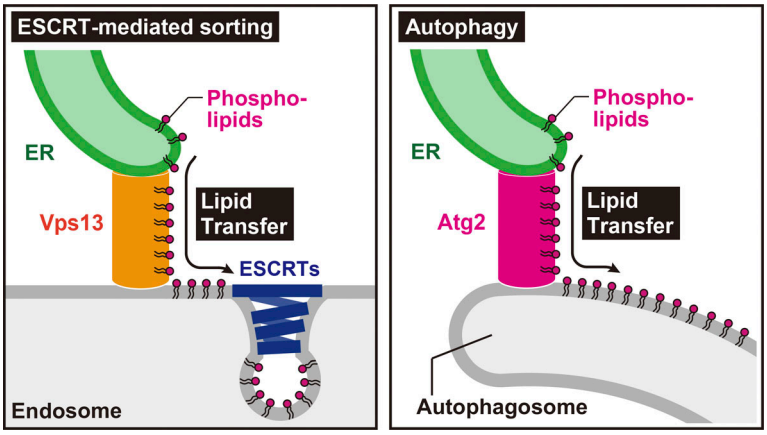

Figure 5. **Model of a role of Vps13 in ESCRT-mediated sorting.** A lipid transfer protein Vps13 may play a critical role in providing lipids to the endosome that permit continuous ESCRT-mediated sorting. During autophagosome formation, Atg2, another Vps13-like lipid transfer protein, delivers lipids from the ER to the autophagosome to support its expansion.

membranes, such as the nuclear membrane, PM, lysosomal membrane, and autophagosome. The bridge-like lipid transfer proteins might contribute to ESCRT-mediated membrane remodeling on diverse organelle membranes. Further studies are required to address this fascinating question and to unravel the precise role of these bridge-like lipid transfer proteins in cellular membrane dynamics.

Materials and methods

Yeast strain and media

Saccharomyces cerevisiae strains used in this study are listed in Table S1. Standard protocols were used for yeast manipulation (Kaiser et al., 1994). Cells were cultured at 26°C to mid-log phase in YNB medium (0.17% [wt/vol] yeast nitrogen base w/o amino acids and ammonium sulfate, 0.5% [wt/vol] ammonium sulfate, and 2% [wt/vol] glucose) supplemented with the appropriate nutrients.

Plasmids

Plasmids used in this study are listed in Table S2.

Antibodies

For immunoblotting, mouse monoclonal anti-GFP (B-2; Sc-9996; Santa Cruz), rabbit polyclonal anti-G6PDH (SAB2100871; Sigma-Aldrich), anti-ubiquitin (P4D1; #3936; Cell Signaling), anti-Pep4 (Klionsky et al., 1988), anti-HA (12CA5; Roche), and anti-Pgk1 (459250; Invitrogen) were used at dilution factors of 1:5,000, 1:10,000, 1:1,000, 1:5,000, 1:5,000, and, 1:10,000, respectively.

AlphaFold structure prediction

For structure prediction of the full-length of *S. cerevisiae* Vps13, we first modeled two segments of Vps13 (1–1,860 and 1,351–3,144 a.a.) by AlphaFold v2.0 and v2.1.1 (Jumper et al., 2021), respectively. Then, using the overlapping region (1,351–1,860 a.a.), we aligned them to generate a full-length structure.

Cargo sorting assay for the ESCRT pathway

For Mup1 sorting, Cells expressing Mup1-GFP were grown in YNB (-Methionine) media to mid-log phase at 26°C and then treated with 20 µg/ml methionine to stimulate Mup1 sorting. For Can1-FKBP sorting, rapamycin-insensitive mutant cells (*tor1-1, fpr1Δ*) expressing Can1-GFP-2xFKBP (Can1-FKBP) and FRB-3xUb were grown to the mid-log phase at 26°C and treated with 200 ng/ml Rapamycin to stimulate its sorting. For the staining with NBD-PC (1-myristoyl-2-{6-[(7-nitro-2-1,3-benzoxadiazol-4-yl)amino]hexanoyl}-sn-glycero-3-phosphocholine; 14:0-06:0 NBD PC, Cat#: 810122P; Avanti Polar Lipids), cells expressing Vph1–mCherry were incubated with 1 mM NBD-PC at 26°C for 30 min. Before imaging, cells were washed with YNB medium three times.

Electron tomography and three-dimensional modeling

Haploid yeast cells were high-pressure frozen and freeze-substituted as previously described (Nickerson et al., 2006; Tseng et al., 2021). Liquid cultures were harvested at the mid-logarithmic phase, vacuum-filtered on 0.45-µm millipore paper, loaded into 0.5-mm aluminum hats, and high-pressure frozen with a Wohlwend HPF (Wohlwend). Cells were freeze-substituted in an Automated Freeze-Substitution machine (AFS) at −90°C in an en bloc preparation of 0.1% uranyl acetate and 0.25% glutaraldehyde in anhydrous acetone. Samples were then washed in pure anhydrous acetone, embedded in Lowicryl HM20 resin (Polysciences), UV polymerized at −60°C warming slowly over 4 d to room temperature. These methods preserve membrane and protein structure and provide consistent en bloc staining (Giddings, 2003, Staehelin communications).

A Leica UC6 Ultra-Microtome was used to cut and place serial sections on Formvar-coated rhodium-plated copper slot grids (Electron Microscopy Sciences). 80-nm thin serial sections were cut for transmission electron microscopy (TEM), and 200-nm thick serial sections were cut for dual-axis tomography. Thin sections were imaged with a FEI Tecnai T12 Spirit electron microscope equipped with a 120-kV LaB6 filament and AMT (2 k × 2 k) CCD. TEM of hundreds of cells per strain was used to quality control freezing, embedding, and staining as done previously (Wilson et al., 2021). Thick sections were labeled with fiduciary 15-nm colloidal gold (British Biocell International) on both sides and tilt imaged with a Tecnai 30 (f-30, 300 kV; FEI-Company) with dual-tilt series images collected from +60° to −60° with 1.5° increments using a Gatan US4000 4 k × 4 k charge-coupled device camera (Abingdon). The tilt series were imaged primarily at 20,000 times magnification and repeated with a 90° rotation to create a dual-axis tomogram with a 3-nm resolution and a 0.4306-nm pixel (Mastronarde, 1997).

Tomograms were built and modeled using the IMOD software package (Kremer et al., 1996, University of Colorado Boulder) using an iMac (Apple). MVB membrane models from dual-axis electron tomograms were manually assigned from the inner leaflet every 5 nm and calculated using IMODmesh. Budding profiles (BPs) were designated by their negative curvature since the majority of endosome-limiting membrane curvature is positive or spherical in shape. BP models are drawn from the 0° rim at the outer leaflet, measured, and sorted by surface area using only BPs that have >750 nm^2 or approximately half of the mean ILV surface (Wemmer et al., 2011). ILVs are spherical and measured using sphere-fitting models from the vesicle's outer leaflet (the inner leaflet of the MVB limiting membrane), and ILV diameters were measured using these sphere models. To determine MVB number and MVB clustering, 100 random cell profiles of WT and *vps13*Δ cells were quantified by thin-section electron microscopy. Videos were made using IMOD and QuickTime Pro (Apple). Data were analyzed and graphed using Prism 9 (GraphPad).

Fluorescence microscopy

Fluorescence microscopy was performed using a CSU-X spinning-disk confocal microscopy system (Intelligent Imaging Innovations) or a DeltaVision Elite system (GE Healthcare Life system).

A CSU-X spinning-disk confocal microscopy system is equipped with a DMI 6000B microscope (Leica), 100×/1.45 numerical aperture objective, and a QuantEM electron-multiplying charge-coupled device (CCD) camera (Photometrics). Imaging of yeast cells was done at room temperature in YNB medium using GFP and mCherry channels with different exposure times according to each protein's fluorescence intensity. Images were analyzed and processed with SlideBook 6.0 software (Intelligent Imaging Innovations).

A DeltaVision Elite system is equipped with an Olympus IX-71 inverted microscope, DV Elite complementary metal-oxide semiconductor camera, a 100×/1.4 NA oil objective, and a DV Light SSI 7 Color illumination system with Live Cell Speed Option with DV Elite filter sets. Imaging was done at room temperature in a YNB medium using GFP, mCherry, and DAPI (for BFP) channels with different exposure times according to each protein's fluorescence intensity. Image acquisition and deconvolution (conservative setting; seven cycles) were performed using DeltaVision software softWoRx 6.5.2 (Applied Precision).

Immunoprecipitation under denature conditions for yeast cell lysate

To analyze the ubiquitination status of Mup1, cells expressing Mup1–GFP were treated with 20 µg/ml methionine for 15 min and washed twice with 400 mM NEM. Cells were lysed in Urea cracking buffer (50 mM Tris-HCl [pH 8.0], 1% SDS, 8 M Urea, 20 mM NEM, 1× protease inhibitor cocktail [Roche]) and lysed by beating with 0.5 mm YZB zirconia beads (Yasui Kikai) for 1 min. High salt IP buffer with 20 mM NEM and 0.2% Triton X-100 was added to the lysate, and the samples were rotated at 4°C for 10 min. The solubilized lysates were cleared at 500 × *g* for 5 min at 4°C, and the resultant supernatants were subjected to high-speed centrifugation at 17,400 × *g* for 10 min. The cleared supernatants were incubated with pre-equilibrated GFP-TRAP_A beads (Chromo Tek) and rotated at 4°C for 1 h. After the beads were washed with SDS wash buffer (50 mM Tris-HCl [pH 8.0], 250 mM NaCl, 1% SDS, 4 M Urea, 5% Glycerol), the bound proteins were eluted by incubating the beads in SDS-PAGE sample buffer at room temperature for 5 min.

Preparation of yeast cell lysate

Cell lysates were prepared as follows: cells were grown to mid-log phase at 26°C. Aliquots of cells were mixed with trichloroacetic acid at a final concentration of 15%, and the mixtures were incubated for 30 min at 4°C. After centrifugation at 17,400 × *g* for 10 min at 4°C, the cells were washed once with 100% acetone and then were lysed in Urea clacking buffer (50 mM Tris-HCl [pH 7.5], 8 M urea, 2% [wt/vol] SDS, and 1 mM EDTA) by beating with 0.5 mm YZB zirconia beads (Yasui Kikai) for 5 min. Then, 2× sample buffer (150 mM Tris-HCl [pH 6.8], 7 M urea, 10% [wt/vol] SDS, 24% [wt/vol] glycerol, and bromophenol blue) was added to the lysate, and the samples were vortexed for 5 min. After centrifugation at 10,000 × *g* for 1 min at room temperature, supernatants were analyzed by SDS-PAGE and immunoblotting using anti-GFP, anti-G6PDH, anti-Pep4, and anti-Pgk1. For quantification of processed GFP from Mup1–GFP and Can1-FKBP, intensity of the band of processed GFP (GFP') at 90 min stimulation was measured. Processed GFP in WT was set to 100%. The data and error bars were obtained from three individual experiments.

Quantitative analysis of cargo localization

The GFP-CPS localization was classified into three categories: (i) vacuole lumen, (ii) vacuole lumen and vacuole membrane, and (iii) vacuole membrane and punctate structure localization. Vps10-GFP and Kex2-GFP localization was classified into three categories: (i) punctate structures, (ii) punctate structure and vacuole membrane, and (iii) vacuole membrane localization. The Pep4-GFP localization was classified into three categories: (i) vacuole lumen, (ii) punctate structures and vacuole lumen, and (iii) punctate structure localization. The Vph1-mCherry localization was classified into three categories: (i) vacuole membrane, (ii) punctate structure and vacuole membrane, and (iii) punctate structure localization. For each experiment, at least 30 cells were classified. The data and error bars were obtained from three independent experiments.

Quantitative analysis of Vps13–GFP localization

Cells having Vps13–GFP punctate structure were quantified. For each experiment, at least 30 cells were classified. The data and error bars were obtained from three independent experiments.

Quantitative analysis of ESCRT localization

GFP-Vps27, Snf7-GFP, and Vps4-GFP puncta colocalizing with mCherry–Vps21 (endosome) was quantified. For each experiment, at least 50 puncta were classified. The data and error bars were obtained from three independent experiments.

Quantitative analysis of Mup1-BFP localization

Mup1-BFP puncta colocalizing with Vps13–GFP (Vps13 positive puncta) and colocalizing with both Vps13–GFP and DsRed–HDEL

were quantified. For each experiment, at least 50 puncta were classified. The data and error bars were obtained from three independent experiments.

Quantitative analysis of Mup1-pHluorin fluorescence at endosomes

The Mup1-pHluorin fluorescence colocalizing with mCherry–Vps21 (served as an endosome marker) was quantified. For each experiment, at least 50 puncta were classified. The data and error bars were obtained from three independent experiments.

Quantitative analysis of NBD-PC fluorescence at the vacuole membrane

The NBD-PC fluorescence colocalizing with Vph1–Cherry (served as a vacuole membrane marker) was quantified. For each experiment, at least 30 cells were classified. The data and error bars were obtained from three independent experiments.

Online supplemental material

Fig. S1 shows the localization of endosomal cargoes in *vps13*Δ cells. Fig. S2 shows Vps13 localization at the ER–endosome contact site. Fig. S3 shows an analysis of ESCRT-mediated sorting in *vps13*Δ cells. Video 1 shows a tomogram of ER–endosome contact sites in *vps4*Δ cells. Video 2 shows the tomogram of an endosome in WT cells. Video 3 shows the tomogram of an endosome in *vps13*Δ cells. Video 4 shows the tomogram of endosomes in *vps13*Δ cells. Table S1 shows yeast strains used in this study. Table S2 shows the plasmids used in this study.

Data availability

Data are available with the article and its supplementary material. Original data, strains, and plasmids generated in this study are available from the corresponding author upon request.

Acknowledgments

We thank all Emr lab members for their helpful discussions. We also thank Dr. Martin Graef (Department of Molecular Biology and Genetics, Cornell University, Ithaca, NY, USA) for sharing plasmids and Dr. Yoshitaka Moriwaki (Department of Biotechnology, Graduate School of Agricultural and Life Sciences, The University of Tokyo, Tokyo, Japan) for critical advice for alphafold2 prediction. S.W. Suzuki is supported by Osamu Hayaishi Memorial Scholarship for Study Abroad.

This work was supported by a Cornell University Research Grant (CU563704) to S.D. Emr.

Author contributions: Conceptualization, S.W. Suzuki; Methodology, S.W. Suzuki; Investigation, S.W. Suzuki, M. West, J.S. Fan, R.T. Roberts, and Y. Zhang; Writing—Original Draft, S.W. Suzuki; Writing—Review and Editing, S.W. Suzuki; Funding Acquisition, S.D. Emr; Resources, S.W. Suzuki; Supervision, S.W. Suzuki.

Disclosures: The authors declare no competing interests exist.

Submitted: 20 July 2023
Revised: 27 December 2023
Accepted: 22 January 2024

References

Bean, B.D.M., S.K. Dziurdzik, K.L. Kolehmainen, C.M.S. Fowler, W.K. Kwong, L.I. Grad, M. Davey, C. Schluter, and E. Conibear. 2018. Competitive organelle-specific adaptors recruit Vps13 to membrane contact sites. *J. Cell Biol.* 217:3593–3607. https://doi.org/10.1083/jcb.201804111

Bilodeau, P.S., J.L. Urbanowski, S.C. Winistorfer, and R.C. Piper. 2002. The Vps27p Hse1p complex binds ubiquitin and mediates endosomal protein sorting. *Nat. Cell Biol.* 4:534–539. https://doi.org/10.1038/ncb815

Carlton, J.G., M. Agromayor, and J. Martin-Serrano. 2008. Differential requirements for Alix and ESCRT-III in cytokinesis and HIV-1 release. *Proc. Natl. Acad. Sci. USA.* 105:10541–10546. https://doi.org/10.1073/pnas.0802008105

Dabrowski, R., S. Tulli, and M. Graef. 2023. Parallel phospholipid transfer by Vps13 and Atg2 determines autophagosome biogenesis dynamics. *J. Cell Biol.* 222:e202211039. https://doi.org/10.1083/jcb.202211039

Dziurdzik, S.K., and E. Conibear. 2021. The Vps13 family of lipid transporters and its role at membrane contact sites. *Int. J. Mol. Sci.* 22:2905. https://doi.org/10.3390/ijms22062905

Friedman, J.R., L.L. Lackner, M. West, J.R. DiBenedetto, J. Nunnari, and G.K. Voeltz. 2011. ER tubules mark sites of mitochondrial division. *Science.* 334:358–362. https://doi.org/10.1126/science.1207385

Gauthier, J., I.A. Meijer, D. Lessel, N.E. Mencacci, D. Krainc, M. Hempel, K. Tsiakas, H. Prokisch, E. Rossignol, M.H. Helm, et al. 2018. Recessive mutations in VPS13D cause childhood onset movement disorders. *Ann. Neurol.* 83:1089–1095. https://doi.org/10.1002/ana.25204

Giddings, T.H. 2003. Freeze-substitution protocols for improved visualization of membranes in high-pressure frozen samples. *J. Microsc.* 212:53–61. https://doi.org/10.1046/j.1365-2818.2003.01228.x

Henne, W.M., N.J. Buchkovich, and S.D. Emr. 2011. The ESCRT pathway. *Dev. Cell.* 21:77–91. https://doi.org/10.1016/j.devcel.2011.05.015

Hurley, J.H. 2015. ESCRTs are everywhere. *EMBO J.* 34:2398–2407. https://doi.org/10.15252/embj.201592484

Jumper, J., R. Evans, A. Pritzel, T. Green, M. Figurnov, O. Ronneberger, K. Tunyasuvunakool, R. Bates, A. Žídek, A. Potapenko, et al. 2021. Highly accurate protein structure prediction with AlphaFold. *Nature.* 596:583–589. https://doi.org/10.1038/s41586-021-03819-2

Kaiser, C., S. Michaelis, and A. Mitchell. 1994. Methods in Yeast Genetics: A Cold Spring Harbor Laboratory Course Manual. Cold Spring Harbor Lab Press, Cold Spring Harbor, NY.

Klionsky, D.J., L.M. Banta, and S.D. Emr. 1988. Intracellular sorting and processing of a yeast vacuolar hydrolase: proteinase A propeptide contains vacuolar targeting information. *Mol. Cell. Biol.* 8:2105–2116. https://doi.org/10.1128/mcb.8.5.2105-2116.1988

Kolehmainen, J., G.C. Black, A. Saarinen, K. Chandler, J. Clayton-Smith, A.L. Träskelin, R. Perveen, S. Kivitie-Kallio, R. Norio, M. Warburg, et al. 2003. Cohen syndrome is caused by mutations in a novel gene, COH1, encoding a transmembrane protein with a presumed role in vesicle-mediated sorting and intracellular protein transport. *Am. J. Hum. Genet.* 72:1359–1369. https://doi.org/10.1086/375454

Kotani, T., H. Kirisako, M. Koizumi, Y. Ohsumi, and H. Nakatogawa. 2018. The Atg2-Atg18 complex tethers pre-autophagosomal membranes to the endoplasmic reticulum for autophagosome formation. *Proc. Natl. Acad. Sci. USA.* 115:10363–10368. https://doi.org/10.1073/pnas.1806727115

Kremer, J.R., D.N. Mastronarde, and J.R. McIntosh. 1996. Computer visualization of three-dimensional image data using IMOD. *J. Struct. Biol.* 116:71–76. https://doi.org/10.1006/jsbi.1996.0013

Kumar, N., M. Leonzino, W. Hancock-Cerutti, F.A. Horenkamp, P. Li, J.A. Lees, H. Wheeler, K.M. Reinisch, and P. De Camilli. 2018. VPS13A and VPS13C are lipid transport proteins differentially localized at ER contact sites. *J. Cell Biol.* 217:3625–3639. https://doi.org/10.1083/jcb.201807019

Lang, A.B., A.T. John Peter, P. Walter, and B. Kornmann. 2015. ER-mitochondrial junctions can be bypassed by dominant mutations in the endosomal protein Vps13. *J. Cell Biol.* 210:883–890. https://doi.org/10.1083/jcb.201502105

Lee, J.A., A. Beigneux, S.T. Ahmad, S.G. Young, and F.B. Gao. 2007. ESCRT-III dysfunction causes autophagosome accumulation and neurodegeneration. *Curr. Biol.* 17:1561–1567. https://doi.org/10.1016/j.cub.2007.07.029

Lesage, S., V. Drouet, E. Majounie, V. Deramecourt, M. Jacoupy, A. Nicolas, F. Cormier-Dequaire, S.M. Hassoun, C. Pujol, S. Ciura, et al. 2016. Loss of VPS13C function in autosomal-recessive parkinsonism causes mitochondrial dysfunction and increases PINK1/parkin-dependent mitophagy. *Am. J. Hum. Genet.* 98:500–513. https://doi.org/10.1016/j.ajhg.2016.01.014

Levine, T.P. 2022. Sequence analysis and structural predictions of lipid transfer bridges in the repeating beta groove (RBG) superfamily reveal past and present domain variations affecting form, function and interactions of VPS13, ATG2, SHIP164, Hobbit and Tweek. *Contact*. 5: 251525642211343. https://doi.org/10.1177/25152564221134328

Li, P., J.A. Lees, C.P. Lusk, and K.M. Reinisch. 2020. Cryo-EM reconstruction of a VPS13 fragment reveals a long groove to channel lipids between membranes. *J. Cell Biol.* 219:e202001161. https://doi.org/10.1083/jcb.202001161

Marcusson, E.G., B.F. Horazdovsky, J.L. Cereghino, E. Gharakhanian, and S.D. Emr. 1994. The sorting receptor for yeast vacuolar carboxypeptidase Y is encoded by the VPS10 gene. *Cell*. 77:579–586. https://doi.org/10.1016/0092-8674(94)90219-4

Mastronarde, D.N. 1997. Dual-axis tomography: An approach with alignment methods that preserve resolution. *J. Struct. Biol.* 120:343–352. https://doi.org/10.1006/jsbi.1997.3919

Melia, T.J., and K.M. Reinisch. 2022. A possible role for VPS13-family proteins in bulk lipid transfer, membrane expansion and organelle biogenesis. *J. Cell Sci.* 135:jcs259357. https://doi.org/10.1242/jcs.259357

Menant, A., R. Barbey, and D. Thomas. 2006. Substrate-mediated remodeling of methionine transport by multiple ubiquitin-dependent mechanisms in yeast cells. *EMBO J.* 25:4436–4447. https://doi.org/10.1038/sj.emboj.7601330

Miesenböck, G., D.A. De Angelis, and J.E. Rothman. 1998. Visualizing secretion and synaptic transmission with pH-sensitive green fluorescent proteins. *Nature*. 394:192–195. https://doi.org/10.1038/28190

Muñoz-Braceras, S., A.R. Tornero-Écija, O. Vincent, and R. Escalante. 2019. VPS13A is closely associated with mitochondria and is required for efficient lysosomal degradation. *Dis. Model. Mech.* 12:dmm036681. https://doi.org/10.1242/dmm.036681

Murley, A., L.L. Lackner, C. Osman, M. West, G.K. Voeltz, P. Walter, and J. Nunnari. 2013. ER-associated mitochondrial division links the distribution of mitochondria and mitochondrial DNA in yeast. *Elife*. 2: e00422. https://doi.org/10.7554/eLife.00422

Nakamura, T.S., Y. Suda, K. Muneshige, Y. Fujieda, Y. Okumura, I. Inoue, T. Tanaka, T. Takahashi, H. Nakanishi, X.D. Gao, et al. 2021. Suppression of Vps13 adaptor protein mutants reveals a central role for PI4P in regulating prospore membrane extension. *PLoS Genet.* 17:e1009727. https://doi.org/10.1371/journal.pgen.1009727

Neuman, S.D., T.P. Levine, and A. Bashirullah. 2022. A novel superfamily of bridge-like lipid transfer proteins. *Trends Cell Biol.* 32:962–974. https://doi.org/10.1016/j.tcb.2022.03.011

Nickerson, D.P., M. West, and G. Odorizzi. 2006. Did2 coordinates Vps4-mediated dissociation of ESCRT-III from endosomes. *J. Cell Biol.* 175: 715–720. https://doi.org/10.1083/jcb.200606113

Osawa, T., T. Kotani, T. Kawaoka, E. Hirata, K. Suzuki, H. Nakatogawa, Y. Ohsumi, and N.N. Noda. 2019. Atg2 mediates direct lipid transfer between membranes for autophagosome formation. *Nat. Struct. Mol. Biol.* 26:281–288. https://doi.org/10.1038/s41594-019-0203-4

Park, J.S., M.K. Thorsness, R. Policastro, L.L. McGoldrick, N.M. Hollingsworth, P.E. Thorsness, and A.M. Neiman. 2016. Yeast Vps13 promotes mitochondrial function and is localized at membrane contact sites. *Mol. Biol. Cell*. 27:2435–2449. https://doi.org/10.1091/mbc.e16-02-0112

Park, J.S., and A.M. Neiman. 2012. VPS13 regulates membrane morphogenesis during sporulation in Saccharomyces cerevisiae. *J. Cell Sci.* 125: 3004–3011. https://doi.org/10.1242/jcs.105114

Rampoldi, L., C. Dobson-Stone, J.P. Rubio, A. Danek, R.M. Chalmers, N.W. Wood, C. Verellen, X. Ferrer, A. Malandrini, G.M. Fabrizi, et al. 2001. A conserved sorting-associated protein is mutant in chorea-acanthocytosis. *Nat. Genet.* 28:119–120. https://doi.org/10.1038/88821

Robinson, J.S., D.J. Klionsky, L.M. Banta, and S.D. Emr. 1988. Protein sorting in Saccharomyces cerevisiae: Isolation of mutants defective in the delivery and processing of multiple vacuolar hydrolases. *Mol. Cell. Biol.* 8: 4936–4948. https://doi.org/10.1128/mcb.8.11.4936-4948.1988

Rusten, T.E., T. Vaccari, K. Lindmo, L.M. Rodahl, I.P. Nezis, C. Sem-Jacobsen, F. Wendler, J.P. Vincent, A. Brech, D. Bilder, and H. Stenmark. 2007. ESCRTs and Fab1 regulate distinct steps of autophagy. *Curr. Biol.* 17: 1817–1825. https://doi.org/10.1016/j.cub.2007.09.032

Russell, M.R., T. Shideler, D.P. Nickerson, M. West, and G. Odorizzi. 2012. Class E compartments form in response to ESCRT dysfunction in yeast due to hyperactivity of the Vps21 Rab GTPase. *J. Cell Sci.* 125:5208–5220. https://doi.org/10.1242/jcs.111310

Rzepnikowska, W., K. Flis, J. Kaminska, M. Grynberg, A. Urbanek, K.R. Ayscough, and T. Zoladek. 2017. Amino acid substitution equivalent to human chorea-acanthocytosis I2771R in yeast Vps13 protein affects its binding to phosphatidylinositol 3-phosphate. *Hum. Mol. Genet.* 26: 1497–1510. https://doi.org/10.1093/hmg/ddx054

Saksena, S., and S.D. Emr. 2009. ESCRTs and human disease. *Biochem. Soc. Trans.* 37:167–172. https://doi.org/10.1042/BST0370167

Seaman, M.N., E.G. Marcusson, J.L. Cereghino, and S.D. Emr. 1997. Endosome to Golgi retrieval of the vacuolar protein sorting receptor, Vps10p, requires the function of the VPS29, VPS30, and VPS35 gene products. *J. Cell Biol.* 137:79–92. https://doi.org/10.1083/jcb.137.1.79

Seaman, M.N., J.M. McCaffery, and S.D. Emr. 1998. A membrane coat complex essential for endosome-to-Golgi retrograde transport in yeast. *J. Cell Biol.* 142:665–681. https://doi.org/10.1083/jcb.142.3.665

Seong, E., R. Insolera, M. Dulovic, E.J. Kamsteeg, J. Trinh, N. Brüggemann, E. Sandford, S. Li, A.B. Ozel, J.Z. Li, et al. 2018. Mutations in VPS13D lead to a new recessive ataxia with spasticity and mitochondrial defects. *Ann. Neurol.* 83:1075–1088. https://doi.org/10.1002/ana.25220

Toulmay, A., F.B. Whittle, J. Yang, X. Bai, J. Diarra, S. Banerjee, T.P. Levine, A. Golden, and W.A. Prinz. 2022. Vps13-like proteins provide phosphatidylethanolamine for GPI anchor synthesis in the ER. *J. Cell Biol.* 221: e202111095. https://doi.org/10.1083/jcb.202111095

Tseng, C.C., S. Dean, B.A. Davies, I.F. Azmi, N. Pashkova, J.A. Payne, J. Staffenhagen, M. West, R.C. Piper, G. Odorizzi, and D.J. Katzmann. 2021. Bro1 stimulates Vps4 to promote intralumenal vesicle formation during multivesicular body biogenesis. *J. Cell Biol.* 220:e202102070. https://doi.org/10.1083/jcb.202102070

Ugur, B., W. Hancock-Cerutti, M. Leonzino, and P. De Camilli. 2020. Role of VPS13, a protein with similarity to ATG2, in physiology and disease. *Curr. Opin. Genet. Dev.* 65:61–68. https://doi.org/10.1016/j.gde.2020.05.027

Valverde, D.P., S. Yu, V. Boggavarapu, N. Kumar, J.A. Lees, T. Walz, K.M. Reinisch, and T.J. Melia. 2019. ATG2 transports lipids to promote autophagosome biogenesis. *J. Cell Biol.* 218:1787–1798. https://doi.org/10.1083/jcb.201811139

Voos, W., and T.H. Stevens. 1998. Retrieval of resident late-Golgi membrane proteins from the prevacuolar compartment of Saccharomyces cerevisiae is dependent on the function of Grd19p. *J. Cell Biol.* 140:577–590. https://doi.org/10.1083/jcb.140.3.577

Wemmer, M., I. Azmi, M. West, B. Davies, D. Katzmann, and G. Odorizzi. 2011. Bro1 binding to Snf7 regulates ESCRT-III membrane scission activity in yeast. *J. Cell Biol.* 192:295–306. https://doi.org/10.1083/jcb.201007018

Wilson, Z.N., D. Buysse, M. West, D. Ahrens, and G. Odorizzi. 2021. Vacuolar H+-ATPase dysfunction rescues intralumenal vesicle cargo sorting in yeast lacking PI(3,5)P2 or Doa4. *J. Cell Sci.* 134:jcs258459. https://doi.org/10.1242/jcs.258459

Yeshaw, W.M., M. van der Zwaag, F. Pinto, L.L. Lahaye, A.I. Faber, R. Gómez-Sánchez, A.M. Dolga, C. Poland, A.P. Monaco, S.C. van Ijzendoorn, et al. 2019. Human VPS13A is associated with multiple organelles and influences mitochondrial morphology and lipid droplet motility. *Elife*. 8: e43561. https://doi.org/10.7554/eLife.43561

Yuan, W., A. Akşit, R. de Boer, A.M. Krikken, and I.J. van der Klei. 2022. Yeast Vps13 is crucial for peroxisome expansion in cells with reduced peroxisome-ER contact sites. *Front. Cell Dev. Biol.* 10:842285. https://doi.org/10.3389/fcell.2022.842285

Zhu, L., J.R. Jorgensen, M. Li, Y.S. Chuang, and S.D. Emr. 2017. ESCRTs function directly on the lysosome membrane to downregulate ubiquitinated lysosomal membrane proteins. *Elife*. 6:e26403. https://doi.org/10.7554/eLife.26403

JCB

Supplemental material

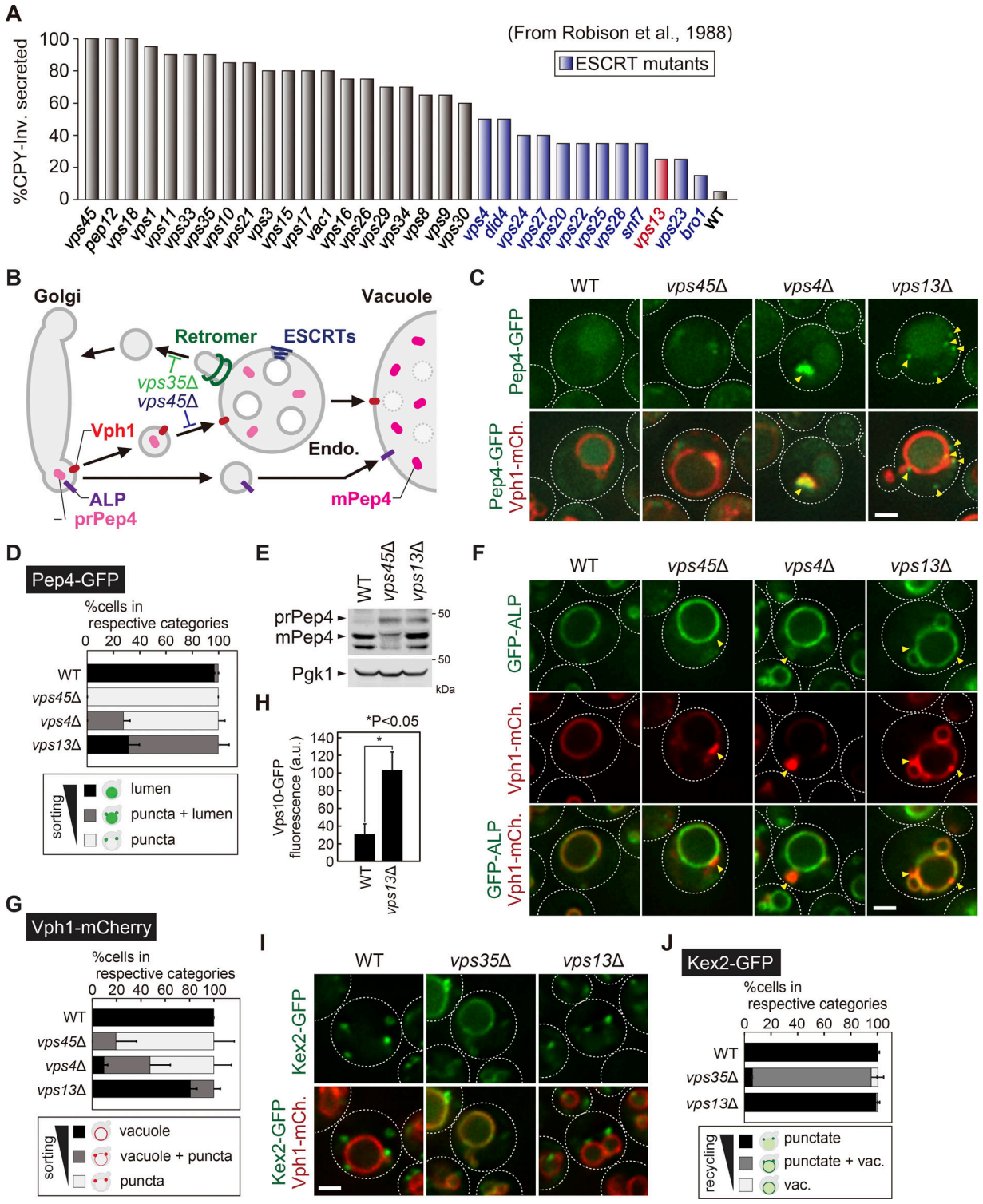

Figure S1. **Endosomal sorting pathways in *vps13Δ* cells. (A)** CPY missorting index in *vps* mutants. The graph represents the percentage of secreted CPY-Invertase as reported by Robison et al. (1988). **(B)** Schematic of vacuolar protein sorting. **(C)** Localization of Pep4–GFP. **(D)** Quantification of Pep4–GFP localization from C. **(E)** Western blotting analysis of Pep4 sorting. Cell lysates were analyzed by immunoblotting using anti-Pep4 and anti-Pgk1 antibodies. **(F)** Localization of GFP–ALP and Vph1–mCherry. **(G)** Quantification of Vph1–mCherry localization from F. **(H)** Quantification of Vps10–GFP fluorescence from Fig. 1 J. **(I)** Kex2–GFP localization in WT, *vps35Δ* (retromer), and *vps13Δ* cells. **(J)** Quantification of Kex2–GFP localization from I. Scale bar: 1 µm. Source data are available for this figure: SourceData FS1.

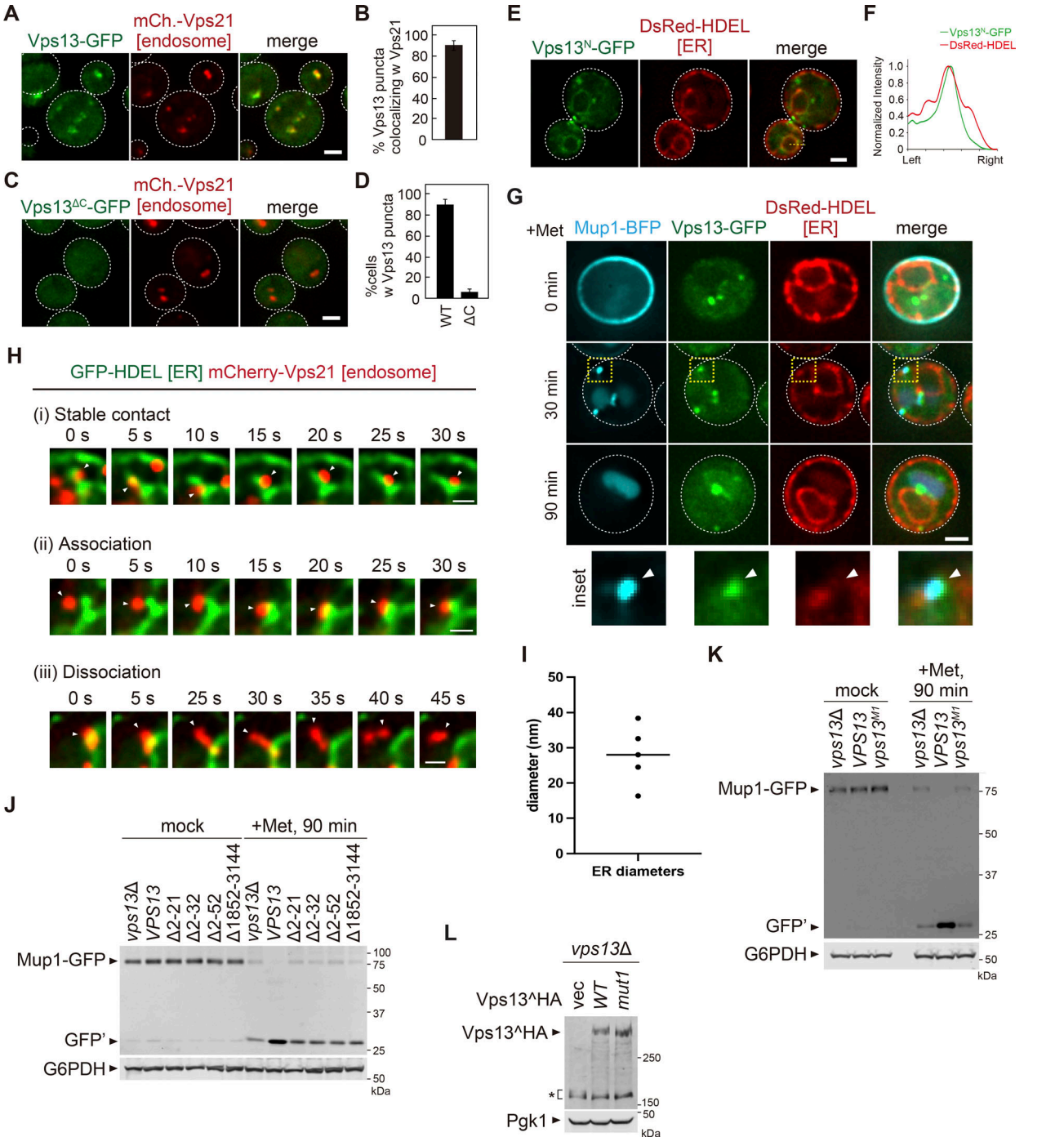

Figure S2. **Vps13 localization at the ER–endosome contact site. (A)** Localization of Vps13–GFP. Scale bar: 1 µm. **(B)** Quantification of Vps13–GFP co-localizing with mCherry–Vps21 from A. **(C)** Localization of Vps13$^{\Delta C}$–GFP (residues 1–1851). Scale bar: 1 µm. **(D)** Quantification of Vps13–GFP puncta localization from C. **(E)** The localization of Vps13^{N}–GFP (residues 1–39). Scale bar: 1 µm. **(F)** Line scan analysis for the region highlighted by the yellow dash line in E. **(G)** Vps13–GFP localization at the ER–endosome contact site. Vps13–GFP, DsRed–HDEL (ER), and Mup1–BFP (endosome) expressing cells were stimulated with methionine. Scale bar: 1 µm. **(H)** Live cell-imaging analysis of the ER (GFP-HDEL) and endosome (mCherry–Vps21). Scale bar: 500 nm. **(I)** The diameter of the ER contact with the endosome. The membrane was designed ER by the observation of its bound ribosomes, dimensions, and staining by high-pressure freezing and electron tomography. ER diameters per 100-nm interval starting at the endosome contact along the 500 nm length of ER were determined. **(J and K)** Mup1–GFP processing in *vps13* mutants after methionine stimulation. Cell lysates were analyzed by immunoblotting using anti-GFP and anti-G6PDH antibodies. **(L)** Western blotting analysis of Vps13 expression. Cell lysates were analyzed by immunoblotting using anti-HA and anti-Pgk1 antibodies. Source data are available for this figure: SourceData FS2.

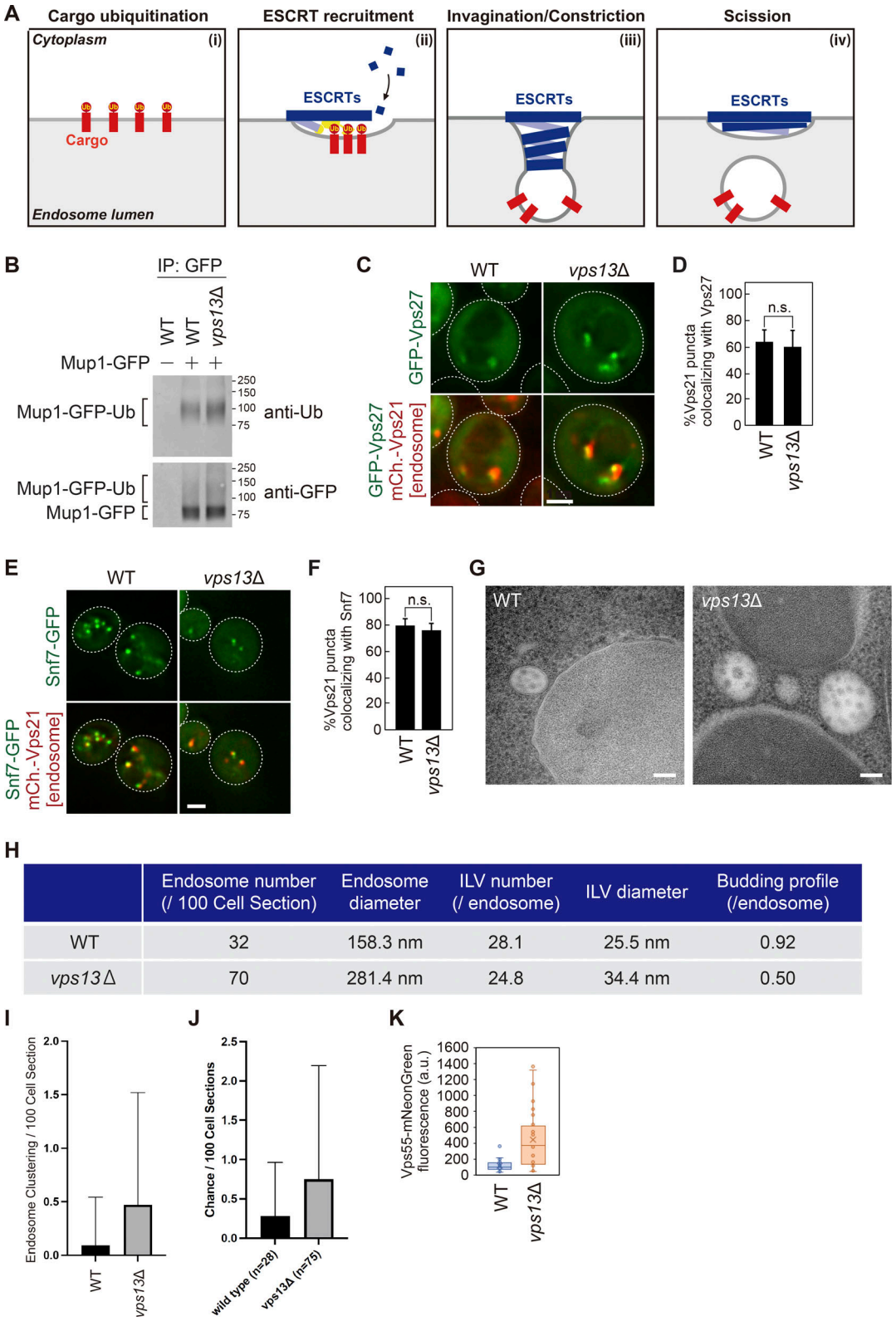

	Endosome number (/ 100 Cell Section)	Endosome diameter	ILV number (/ endosome)	ILV diameter	Budding profile (/endosome)
WT	32	158.3 nm	28.1	25.5 nm	0.92
vps13Δ	70	281.4 nm	24.8	34.4 nm	0.50

Figure S3. **Characterization of MVB biogenesis in *vps13* mutants. (A)** Schematic of ESCRT-mediated sorting at the endosome. **(B)** The ubiquitination of Mup1–GFP. Mup1–GFP expressing cells were stimulated with methionine for 15 min and then immunoprecipitated under denatured conditions. The immunoprecipitated (IP) products were analyzed by immunoblotting using anti-GFP and anti-ubiquitin antibodies. **(C)** GFP–Vps27 (ESCRT-0) localization. Scale bar: 1 µm. **(D)** Quantification of GFP–Vps27 localization from C. **(E)** Snf7–GFP (ESCRT-III) localization. Scale bar: 1 µm. **(F)** Quantification of Snf7–GFP localization from E. **(G)** Thin section electron miscopy images of WT and *vps13Δ* yeast cells. Scale bars: 100 nm. **(H)** The value of quantification data of electron tomography analysis. **(I)** Quantification of endosome clustering. **(J)** Quantification of the chance of MVBs (endosomes) in WT and *vps13Δ* cells. **(K)** Fluorescence intensity of the Vps55–mNeonGreen punctate structures from Fig. 4 D. Source data are available for this figure: SourceData FS3.

Video 1. **Tomogram of ER–endosome contact sites in *vps4Δ* cells.** ER is shown in green. Ribosomes are indicated as green dots. The endosome stacks are shown in different colors to differentiate individual membranes. Round endosomes are traced in yellow. Larger tubular and cisternal structures are in various shades. Scale bar: 100 nm.

Video 2. **Tomogram of an endosome in WT cells.** The wild-type endosome contains the intraluminal vesicle (ILV). The limiting endosomal membrane is shown in yellow. The ILVs are in red. Scale bar: 100 nm.

Video 3. **Tomogram of an endosome in *vps13Δ* cells.** The limiting endosomal membrane is shown in yellow. The ILVs are in red. Scale bar: 100 nm.

Video 4. **Tomogram of endosomes in *vps13Δ* cells.** The limiting endosomal membrane is shown in yellow. The ILVs are in red. Scale bar: 100 nm.

Provided online are Table S1 and Table S2. Table S1 shows yeast strains used in this study. Table S2 shows plasmids used in this study.